

CrystEngComm

Accepted Manuscript



This is an *Accepted Manuscript*, which has been through the Royal Society of Chemistry peer review process and has been accepted for publication.

Accepted Manuscripts are published online shortly after acceptance, before technical editing, formatting and proof reading. Using this free service, authors can make their results available to the community, in citable form, before we publish the edited article. We will replace this *Accepted Manuscript* with the edited and formatted *Advance Article* as soon as it is available.

You can find more information about *Accepted Manuscripts* in the [Information for Authors](#).

Please note that technical editing may introduce minor changes to the text and/or graphics, which may alter content. The journal's standard [Terms & Conditions](#) and the [Ethical guidelines](#) still apply. In no event shall the Royal Society of Chemistry be held responsible for any errors or omissions in this *Accepted Manuscript* or any consequences arising from the use of any information it contains.

**In-situ Neutron Powder Diffraction Study of the Reaction
 $M_2O_3 \leftrightarrow M_3O_4 \leftrightarrow MO$, $M = (Fe_{0.2}Mn_{0.8})$: Implications for
Chemical Looping with Oxygen Uncoupling.**

S.T. Norberg^{1,2}, G. Azimi¹, S. Hull², and H. Leion¹.

¹ Department of Chemistry and Chemical Engineering, Chalmers University of Technology,
SE-412 96 Gothenburg, Sweden.

² The ISIS Facility, STFC Rutherford Appleton Laboratory, Chilton, Didcot, Oxfordshire,
OX11 0QX, United Kingdom.

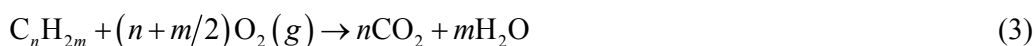
Corresponding Author: Stefan T. Norberg.
Address: Department of Chemistry and Chemical Engineering, Chalmers
University of Technology, SE-412 96 Gothenburg, Sweden.
Tel: int + 46 31 772 2876
E-mail: stn@chalmers.se

Abstract.

The structural properties of $(\text{Fe}_{0.2}\text{Mn}_{0.8})_x\text{O}_y$ as a function of temperature under differing oxidizing and reducing atmospheres have been investigated using thermal gravimetric analysis and neutron powder diffraction techniques. The principal observation is a reversible transition between the (low temperature) bixbyite and (high temperature) cubic spinel structured phases, which occurs over a significant temperature range and is dependent on the surrounding gas atmosphere. In addition to detailed information concerning the temperature dependence of the positional parameters, analysis of the powder neutron diffraction data shows that the two metal species are not completely randomly distributed over the two symmetry independent cation sites within the bixbyite and cubic spinel phases. More significantly, the two phases appear to be completely stoichiometric, with compositions $(\text{Fe}_{0.2}\text{Mn}_{0.8})_2\text{O}_3$ and $(\text{Fe}_{0.2}\text{Mn}_{0.8})_3\text{O}_4$, respectively. Under severely reducing conditions, the sample transforms to a rocksalt structured phase of stoichiometry $(\text{Fe}_{0.2}\text{Mn}_{0.8})_x\text{O}_y$, but reverts to the spinel and bixbyite phases on re-oxidation. The implications of these findings for the use of $(\text{Fe}_{1-x}\text{Mn}_x)\text{O}_y$ as oxygen carriers in Chemical Looping Combustion (CLC) and Chemical Looping with Oxygen Uncoupling (CLOU) techniques to capture CO_2 during combustion of hydrocarbon fuels is briefly discussed.

1. Introduction.

Chemical-looping with Oxygen Uncoupling (CLOU) is a technique for capturing CO₂ during combustion of fuels such as natural gas, coal or biomass, and is of great interest for the potential benefits of separating fuel reactor CO₂ and H₂O from excess O₂ and N₂. By eliminating the need for separation of gases, costly and energy consuming equipment is avoided [1]. The CLOU system is composed of two fluidized bed reactors (Figure 1). One of them is an air reactor where a solid oxygen carrier, usually a metal oxide, is oxidized by air (reaction (1)). The oxygen carrier is then transported to the second reactor, the fuel reactor. In the fuel reactor, the oxygen carrier material releases gas phase O₂ (reaction (2)) and then added fuel reacts with the gaseous oxygen to produce CO₂ and H₂O (reaction (3)). The reduced oxygen carrier is then transported back to the air reactor to be re-oxidized to its original state. The total amount of heat released from the fuel reactor and the air reactor is equal to the heat released from normal combustion [1]. The product gases from the fuel reactor consist almost only of CO₂ and H₂O. The H₂O can be condensed and pure CO₂ can be compressed and transported to an appropriate storage location. The product gases from the air reactor consist mainly of nitrogen and a small amount of oxygen which can be released to the atmosphere.



The system Fe-Mn-O appears to be especially promising due to favourable thermodynamics [2,3] which are also confirmed by experimental work [4,5]. Figure 2 shows a phase diagram of the (Fe_{1-x}Mn_x)O_y system, calculated using the FactSage software and accompanied FToxid database [6,7], for a partial pressure of 5% O₂ (roughly corresponding to the exiting O₂ concentration from the air reactor). The stable phases at low temperature are hematite and bixbyite, both with the general formula (Fe_{1-x}Mn_x)₂O₃, whereas the spinel phase (Fe_{1-x}Mn_x)₃O₄ is stable at high temperature. There are also two-phase areas in which both forms *i.e.* bixbyite/hematite and spinel, coexist at intermediate temperatures. Moving from low to high temperatures will give a phase change from (Fe_{1-x}Mn_x)₂O₃ to (Fe_{1-x}Mn_x)₃O₄ which is accompanied by oxygen release (reaction (4)) equivalent to 3.37% change of mass. A similar release of O₂ is expected to occur when moving from a high to a low partial pressure of oxygen, very similar to the situation when an oxygen carrier is transported from the air to the fuel reactor of a CLOU-system.

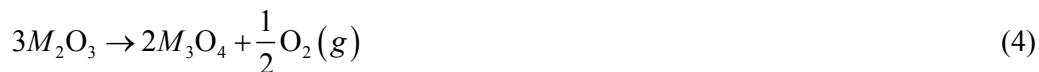


Figure 2 shows that, as Mn and Fe are mixed, the phase transition between fully oxidized phase $(Fe_{1-x}Mn_x)_2O_3$ and fully reduced phase needs to pass a two phase area where both phases coexist. This means that, for a constant oxygen partial pressure, a certain temperature change is needed to accomplish the phase change between the fully oxidized and fully reduced phases. The same will also apply to the change in oxygen concentration, if a change in oxygen concentration is used to achieve this phase change at constant temperature. Figure 2 also indicates that the smallest change is needed where the manganese fraction is $0.6 \leq x \leq 0.8$.

X-ray powder diffraction has been used to probe the structural behaviour of the Fe-Mn-O system [4,5]. However, it is difficult to differentiate between iron and manganese using X-ray methods, as these elements are neighbours in the periodic table. Furthermore, the scattering factor for oxygen is much smaller than that of the cations, making it difficult to accurately assess the oxygen content. Therefore, Neutron Powder Diffraction has been used in this work to investigate the structural properties of $(Fe_{0.2}Mn_{0.8})_xO_y$ as a function of temperature under differing oxidizing and reducing atmospheres.

2. Experimental Details.

The oxygen carrier studied in this work has the composition $(Fe_{1-x}Mn_x)O_y$ with $x=0.8$ and was produced by spray drying at VITO in Belgium. Powder mixtures of Mn_3O_4 (supplied by Chemalloy) and Fe_2O_3 (supplied by Alfa Aesar) were dispersed in deionized water containing organic additives. Polyethyleneoxide (PEO, type PEO-1 Sumitomo Seika, Japan) and/or polyvinylalcohol (PVA 1500 Fluka, Switzerland) and/or polyethyleneglycol (PEG 6000, Merck-Schuchardt, Germany) were used as organic binder, Darvan (type C, RT Vanderbilt, USA) and/or Dolapix (types A88, PC75 and PC80, Zschimmer & Schwarz, Germany) and/or Targon 1128 (BK Giulini Chemie, Germany) were used as dispersants. The water-based suspension was continuously stirred with a propeller blade mixer while being pumped to the 2-fluid spray-dry nozzle, positioned in the lower cone part of the spray-drier. After spray-drying, the fraction within the required particle size range was sieved to separate it from the rest of the spray-dried product. In order to obtain oxygen carrier particles with sufficient mechanical strength, calcination was performed in air at 950 and 1100°C, for 4 h. After calcination, the particles were sieved again to the size range 125-180 µm

[8]. These particles were used in the TGA experiments whereas a porous pellet was then pressed from the particles and used during the neutron diffraction experiments.

Thermal Gravimetric Analysis (TGA) measurements were performed on a NETZSCH model STA 409 PC Luxx simultaneous thermal analyzer. This system uses an SiC furnace which operates between 25 and 1550°C and a TG-DSC sensor with a resolution of 2µg/digit. The apparatus includes two crucibles, one to act as reference and another to hold the sample. So, the empty sample holder's weight is determined first after which the sample, usually of mass between 50 and 100mg, is loaded and weighed. The instrument is evacuated and purged twice with N₂ prior to measurements. The flowing gas always includes protective N₂, and is stabilized for 10 to 20 minutes prior to each measurement. The sample is exposed to an atmosphere of 5% O₂ in nitrogen, with a protective N₂ flow (20mL/min).

Before the neutron diffraction experiments the (Fe_{0.2}Mn_{0.8})_xO_y pellet was loosely crushed and stacked vertically on top of a porous silica glass frit within a silica glass tube of wall thickness 0.5mm. This tube passes vertically through the hot zone of a resistive heating furnace designed for neutron powder diffraction experiments, constructed using vanadium foil heating element and heat shields. All measurements were performed with gas flowing through the silica tube at a rate of 80mL/min. Gas mixtures of 100%Ar, 5%O₂-95%Ar, 21%O₂-79%Ar and CO were used to provide variable reducing/oxidizing atmosphere around the sample pellets, with the gas flow and composition controlled by a gas panel (Hastings 300 series mass flow controllers) interfaced to the control PC of the diffractometer. The temperature within the silica tube was monitored using type K thermocouples situated above and below the pellets. A full description of the sample cell, gas panel and control system can be found elsewhere [9].

The diffraction experiments were performed using the Polaris powder diffractometer at the ISIS Facility, Rutherford Appleton Laboratory, U.K. [10]. Diffraction data were collected using the backscattering detector bank which covers the scattering angles 130°<2θ<160°, providing data over the *d*-spacing range 0.2<*d*(Å)<3.2 with a resolution Δ*d*/*d*~5×10⁻³. Diffraction data were typically collected for approximately 15 min at each temperature/gas flow. This provided data of sufficient statistical quality to allow Rietveld profile refinement of the data to be performed using the GSAS software [11], to extract the lattice parameter, positional parameters, site occupancy factors and isotropic thermal vibration parameters. Additional fitted parameters for each detector bank comprised a scale factor, peak width parameters describing Gaussian and Lorentzian contributions to the Bragg profile and the coefficients of 15-th order shifted Chebyshev polynomial function to

describe the background scattering, which predominantly arises from the silica glass tube. The overall Fe:Mn cation ratio of 4:1 was included as a constraint in all refinements, whilst allowing individual cation sites to each possess occupancies which differ from this value. The oxygen occupancy of the anion sites was allowed to vary away from the nominal value expected for the stoichiometry of the phase under investigation, to probe any oxygen loss/gain associated with changes in valence of the cations.

3. Results.

3.1. Thermal Gravimetric Analysis.

A typical Thermal Gravimetric trace is shown in figure 3, for the sample of $(\text{Fe}_{0.21}\text{Mn}_{0.79})_2\text{O}_3$ heated in a 5% O_2 atmosphere. As the temperature rises steadily to 1110°C , the sample starts to lose weight at temperatures of 925°C , due to O_2 release from the oxygen carrier. The sample loses around 3.5 wt%, before the temperature reaches around 1020°C . This is very close to the expected weight loss of 3.3-3.4% for the decomposition of bixbyite structured $(\text{Fe}_{0.21}\text{Mn}_{0.79})_2\text{O}_3$ to spinel structured $(\text{Fe}_{0.21}\text{Mn}_{0.79})_3\text{O}_4$.

3.2. Crystal Structures.

Before presenting the results of the neutron powder diffraction studies, it is instructive to briefly consider the crystal structures of the phases present in the $(\text{Fe}_{1-x}\text{Mn}_x)\text{O}_y$ system. As the two cation species readily adopt valences of Fe^{2+} , Fe^{3+} , Mn^{2+} , Mn^{3+} and Mn^{4+} , the end members Fe_xO_y and Mn_xO_y show different stoichiometries and structure types even under ambient conditions. Fe^{2+}O and Mn^{2+}O adopt the cubic rocksalt structure (space group $Fm\bar{3}m$), whilst $\text{Fe}_2^{3+}\text{O}_3$ can be prepared in four different forms, including α (hematite, rhombohedral $R\bar{3}c$), β (cubic bixbyite structure, $Ia\bar{3}$) and γ (maghemite, cubic spinel structure, $Fd\bar{3}m$) and $\text{Mn}_2^{3+}\text{O}_3$ in two forms, α (orthorhombic distortion of the bixbyite structure, $Pbca$) and γ (spinel related). In the mixed valence compounds, $(\text{Fe}_2^{2+}\text{Fe}_2^{3+})\text{O}_3$ (magnetite) and $(\text{Mn}_2^{2+}\text{Mn}_2^{3+})\text{O}_3$ (hausmannite) adopt the cubic spinel structure and a tetragonal distorted form of it ($I4_1/amd$), respectively, whilst Mn^{4+}O_2 has several polymorphs, including rutile and hollandite structured forms.

For the purposes of this paper, the most relevant structures to consider in more detail are the rocksalt, spinel (*S*) and bixbyite (*B*) structures (where the labels refer to the phase diagram, figure 2). In common with many structure types adopted by compounds characterised by predominantly ionic bonding, these arrangements can be derived by filling some, or all, of the octahedral and/or tetrahedral interstices formed by a close packed sublattice of counter ions - face centred cubic (*f.c.c.*) in the three cases considered here. In the rocksalt structure, both the anions and cations adopt *f.c.c.* sublattices, whilst anions and cations form the *f.c.c.* sublattices in the case of spinel and bixbyite structures, respectively. The crystallographic descriptions of the idealised form of the three structures are given in table 1 though, in practice, small displacements away from the ideal *x*, *y* and *z* values given for the various positional parameters occur in the spinel and bixbyite cases. More realistic representations of the structures are shown in figure 4.

3.3. Neutron Powder Diffraction.

In its 'as prepared' form, the $(\text{Fe}_{0.2}\text{Mn}_{0.8})_x\text{O}_y$ sample comprised of a mixture of the bixbyite (*B*) and spinel (*S*) structured phases, of approximate weight ratio 4:1. A typical thermodiffraction is shown in figure 5. The results of these temperature scans to probe the phase stabilities under different atmosphere are illustrated in figure 6. On heating under an inert atmosphere of 100%Ar the sample transforms to a pure spinel phase over the temperature range 830-940°C. Cooling under 5%O₂-95%Ar led to the reappearance of the bixbyite phase at 760-800°C. Starting with a pure spinel structured material at 1000°C, cooling under an oxidizing atmosphere of 21%O₂-79%Ar led to a complete transformation to the bixbyite phase over the temperature range 850-900°C, whilst the reverse transformation occurred on heating over the range 960-1010°C. Repeating this process under an atmosphere of 5%O₂-95%Ar produced only a partial transformation from the spinel to the bixbyite phase (around 20% conversion, by weight) down to the lowest temperature used (750°C). On heating, complete transformation back to the spinel phase occurred over the temperature range 900-950°C.

To further test the stability of $(\text{Fe}_{0.2}\text{Mn}_{0.8})_x\text{O}_y$ under reducing conditions, the sample in its pure spinel form was exposed to bursts of pure CO gas flow for 3 periods of 2 minutes at a temperature of 848°C. As shown in figure 7, this led to a reduction of the material to a rocksalt structured phase which, on re-oxidizing at 760°C, converted back to the bixbyite and spinel phases.

3.4. Structural Refinements.

A detailed characterisation of the crystal structures of the three phases encountered in this work used Rietveld refinement of neutron powder data collected at 802(2)°C under 21%O₂-79%Ar for bixbyite structured (Fe_{0.2}Mn_{0.8})₂O₃, at 1005(2)°C under 21%O₂-79%Ar for spinel structured (Fe_{0.2}Mn_{0.8})₃O₄ and at 848(2)°C under 100%CO for rocksalt structured (Fe_{0.2}Mn_{0.8})O as, under these conditions, each phase exists in its pure form. The results are summarised in table 2 and the quality of the fits to the neutron powder diffraction data for the three phases is illustrated in figure 8 and by the R_{wp} -factors in table 2.

In the case of the bixbyite phase, there are two cation sites $M1$ and $M2$, with the single variable positional parameter of the latter refining to a value $x_{M2}=0.2822(8)$ close to value of $1/4$ which would, together with the $M1$ sites, form an ideal *f.c.c.* sublattice. The O positions are somewhat displaced from their ideal $x_O=1/8$, $y_O=3/8$, $z_O=1/8$ positions, such that the anion co-ordination around the $M1$ cations can be considered to be a cube with two corners vacancy. However, whilst the co-ordination around the $M2$ cations is also 6-fold, the environment is much more distorted, as shown by the $M2$ -O bond lengths and O- $M2$ -O bond angles in table 2.

There are also two symmetry independent cation sites within the cubic spinel structure, where the $M1$ and $M2$ sites are located in the *tet1* and *oct2* interstices of the *f.c.c.* anion sublattice, respectively (see table 1). The solitary variable positional parameter is that of the O anions which form the *f.c.c.* sublattice, and its slight deviation from the ideal value of $x_O=1/4$ means the O- $M2$ -O angles for the octahedrally co-ordinated cations differ slightly from 90°, though the $M1$ co-ordination environment remains a perfect tetrahedron.

In both the bixbyite and spinel phases, the possibility that the Fe/Mn preferentially occupy one of the two cation sites was explored. In each case, a slight, but statistically significant, deviation from a purely random distribution was observed, producing a significant improvement in the quality of the fit to the neutron powder diffraction data. In the bixbyite case, Mn has a slight preference for the more distorted $M2$ sites, whilst in spinel these cations show a slight tendency to occupy the tetrahedrally co-ordinated $M1$ sites rather than the octahedrally co-ordinated $M2$ positions.

The rocksalt structure contains no variable positional parameters and the octahedral co-ordination of the anions within an ideal *f.c.c.* array of cations (and of cations within an *f.c.c.* array of anions) is constrained by symmetry.

It is important to note that attempts to vary the oxygen content within the unit cells did not produce any significant improvement in the quality of fit in any of the three phases. The structural descriptions given in table 2 were thus used as the starting models for the analysis of all the neutron powder diffraction data collected under differing gas flows and temperatures. The results of this analysis are shown in figures 9 to 13.

4. Discussion.

Considering first the structural behaviour of the bixbyite structured $(\text{Fe}_{0.2}\text{Mn}_{0.8})_2\text{O}_3$ and spinel structured $(\text{Fe}_{0.2}\text{Mn}_{0.8})_3\text{O}_4$ with temperature shown in figures 9 to 13, there is no evidence of any significant differences between the structural descriptions of either phase when measured at the same temperature under different gas atmospheres. This is clear, for example, for the temperature dependence of the volume per formula unit shown in figure 9 and supports the major conclusion of this work - that the structural transition occurs between essentially stoichiometric phases at a temperature which varies with oxygen partial pressure of the surrounding atmosphere.

As discussed in section 3.2 and detailed in table 1, the crystal structures of the idealised bixbyite and spinel structures can be described in terms of an *f.c.c.* sublattice (of cations and anions, respectively), in which the counterions occupy tetrahedral and/or octahedral interstices. In reality, there are slight displacements of some of the ions away from the ideal positions, leading to minor distortions of the *f.c.c.* sublattice and non-ideal polyhedral units. In the case of the bixbyite structure, the *f.c.c.* sublattice is comprised of cations on the *M1* and *M2* positions and, as shown in figure 10, the only positional parameter, x_{M2} , decreases with increasing temperature, tending towards the ideal value of $x_{M2}=1/4$. The anions, which occupy $3/4$ of all the available tetrahedral cavities, occupy the general 24-fold positions, also show a slight tendency towards the ideal geometry by showing an increase in x_{O} , a very slight increase in y_{O} and a significant decrease in z_{O} with temperature, towards the perfect values of $1/8$, $3/8$ and $1/8$, respectively (see figure 10). A similar observation is made for the spinel structured phase, with the only variable positional parameter being the x-co-ordinate of the anions which form the *f.c.c.* sublattice which decreases slightly with increasing temperature towards the ideal value of $x_{\text{O}}=1/4$. Perhaps the most surprising result of the analysis of the powder neutron diffraction data is the non-random distribution of the two cation species, Fe and Mn, over the two cation sites within the crystal structures of both the spinel and bixbyite phases. However, as shown in figure 11, the distribution tends towards a more random arrangement with increasing temperature.

Before discussing the implications of these findings for the use of the material within CLOU reactors, it is instructive to compare the results provided by the TGA and NPD techniques. In the latter case, it is possible to use the temperature variation of the weight fractions of the bixbyite and spinel structured phases determined by the Rietveld refinements of the diffraction data (figure 6) to calculate the change in sample mass with temperature. By recasting the TGA data in the form of mass versus temperature (rather than time), it is then possible to make a direct comparison and, as shown for the case of heating under a 5% atmosphere in figure 3, an excellent agreement is obtained.

In summary, these results confirm that the materials are combined oxides of iron and manganese which exist in 3 crystal structures of $(\text{Fe}_{0.2}\text{Mn}_{0.8})_2\text{O}_3$, $(\text{Fe}_{0.2}\text{Mn}_{0.8})_3\text{O}_4$ and $(\text{Fe}_{0.2}\text{Mn}_{0.8})\text{O}$. These crystal structures were also seen in the experiments in batch fluidized bed reactor reported by [5,12]. Here the results are generally in line with the results of CLOU experiments in a batch fluidized bed reactor. The work by Azimi *et al* [5,12] involved decomposition of the oxygen carrier in nitrogen at 850°C, where the sample released O_2 . This is similar to the neutron diffraction experiments conducted here with Ar. Both showed oxygen release due to decomposition of bixbyite to spinel during under inert conditions. In both cases the materials were oxidized with 5% O_2 . For the fluidized bed experiments, the oxidation was slow at 850°C and in the TGA experiments presented above the materials could not be fully oxidized back to bixbyite. In the neutron diffraction experiments 21% O_2 was also applied instead of 5% O_2 during oxidation, the materials could then be completely oxidized back to bixbyite.

$(\text{Mn,Fe})_2\text{O}_3$ has been shown to completely convert to $(\text{Mn,Fe})_3\text{O}_4$ in an inert atmosphere, which can be further reduced to $(\text{Mn,Fe})\text{O}$ if a stronger reducing agent such as CO is used. However, this further reduction cannot release O_2 in its gas phase, and is not capable of providing complete conversion of CO or CH_4 to CO_2 and H_2O [5]. Even so, in a commercial large scale CLOU unit it is likely that certain fuel rich spots can occur that accidentally over reduce the oxygen carrier to $(\text{Mn,Fe})\text{O}$.

There have been several attempts to determine the kinetics for the O_2 release from CLOU materials. The problem has been that the O_2 partial pressure around the material has a strong influence on the rate [13]. In some cases, the apparent kinetics of CLOU have been determined [5,14], but the mechanism of the reaction is not known. The fact that the two phases $(\text{Fe}_{0.2}\text{Mn}_{0.8})_2\text{O}_3$ and $(\text{Fe}_{0.2}\text{Mn}_{0.8})_3\text{O}_4$ appear to be completely stoichiometric provides important information, but is

insufficient to unambiguously determine the mechanism for O₂ release. However, it does demonstrate that the oxygen transfer in the material is relatively rapid and makes, for example, makes a description based on a shrinking core mechanism less probable.

5. Conclusions.

This work confirms that a combined iron manganese oxide with a Fe:Mn ratio of 1:4 exists in three distinct phases - bixbyite-structured (Fe_{0.2}Mn_{0.8})₂O₃, spinel-structured (Fe_{0.2}Mn_{0.8})₃O₄ and rocksalt-structured (Fe_{0.2}Mn_{0.8})O. When exposed to an inert atmosphere, the (Fe_{0.2}Mn_{0.8})₂O₃ phase undergoes a weight loss of 3.5 wt%, at temperatures up to 1020°C, which is consistent with the expected weight loss of 3.3-3.4% for the decomposition of a bixbyite-structured phase to a spinel-structured modification. Whilst the neutron powder diffraction studies are highly sensitive to the oxygen content within the material, there is no evidence for this work that either phase shows significant departures from their nominal M₂O₃ and M₃O₄ stoichiometries, respectively.

In terms of their more detailed crystallographic characterisations, both the bixbyite and spinel phases show a slight, but statistically significant, deviation from a purely random distribution. In the bixbyite case, Mn has a slight preference for the more distorted M₂ sites, whilst in spinel phase these cations show a slight tendency to occupy the tetrahedrally co-ordinated M₁ sites. However, the distribution tends towards a more random arrangement with increasing temperature. The latter is consistent with the analysis of the temperature dependence of the positional parameters, as each phase tends towards a more symmetric arrangement on increasing temperature.

After the sample had been reduced with CO to form a rocksalt-structured (Fe_{0.2}Mn_{0.8})O phase, it was possible to completely regain the spinel and bixbyite phases by oxidation. As discussed above, this is likely to prove beneficial for the use of (Fe_{1-x}Mn_x)O_y as oxygen carriers in Chemical Looping Combustion (CLC) and Chemical Looping with Oxygen Uncoupling (CLOU).

Acknowledgements.

The authors wish to thank Richie Haynes (ISIS) for assistance with the collection of the neutron powder diffraction data. The UK Science and Technology Facilities Council is thanked for allocating neutron beamtime at the ISIS Facility. STN wishes to thank Vetenskapsrådet (The Swedish Research Council) for financial support. HL wishes to thank Formas for financial support.

References.

- [1] T. Mattisson, A. Lyngfelt and H. Leion, "Chemical-looping with oxygen uncoupling for combustion of solid fuels", *Int. J. Greenh. Gas Con.*, **3**, 11-19 (2009).
- [2] J.V. Crum, B.J. Riley and J.D. Vienna, "Binary phase diagram of the manganese oxide-iron oxide system", *J. Am. Ceram. Soc.*, **92**, 2378-2384 (2009).
- [3] D. Wickham, "The chemical composition of spinels in the system $\text{Fe}_3\text{O}_4\text{-Mn}_3\text{O}_4$ ", *J. Inorg. Nucl. Chem.*, **31**, 313-320 (1969).
- [4] G. Azimi, H. Leion, M. Rydén, T. Mattisson and A. Lyngfelt, "Investigation of different Mn-Fe oxides as oxygen carrier for chemical-looping with oxygen uncoupling (CLOU)", *Energ. Fuels*, **27**, 367-377 (2013).
- [5] G. Azimi, M. Rydén, H. Leion, T. Mattisson and A. Lyngfelt, " $(\text{Mn}_z\text{Fe}_{1-z})_y\text{O}_x$ combined oxides as oxygen carrier for chemical-looping with oxygen uncoupling", *Am. Inst. Chem. Eng. J.*, **59**, 582-588 (2013).
- [6] C. Bale, P. Chartrand, S. A. Degterov, G. Eriksson, K. Hack, R. Ben Mahfoud, J. Melancon, A. D. Pelton and S. Petersen, "FactSage thermochemical software and databases", *CALPHAD*, **29**, 189-228 (2002)
- [7] C. W. Bale, E. Belisle, P. Chartrand, S. A. Decterov, G. Eriksson, K. Hack, I. H. Jung, Y. B. Kang, J. Melancon, A. D. Pelton, C. Robelin and S. Petersen, "FactSage thermochemical software and databases - recent developments", *CALPHAD*, **33**, 295-311 (2009)
- [8] E. Jerndal, T. Mattisson, I. Thijs, F. Snijkers and A. Lyngfelt, "Investigation of NiO/NiAl₂O₄ oxygen carriers for chemical-looping combustion produced by spray-drying", *Int. J. Greenh. Gas Con.*, **4**, 23-35 (2010).
- [9] R. Haynes, S.T. Norberg, S.G. Eriksson, M.A.H. Chowdhury, C.M. Goodway, G.D. Howells, O. Kirichek and S. Hull, "New high temperature gas flow cell developed at ISIS", *J. Phys.: Conf. Ser.*, **251**, 012090 (2010).
- [10] S. Hull, R.I. Smith, W.I.F. David, A.C. Hannon, J. Mayers and R. Cywinski, "The Polaris powder diffractometer at ISIS", *Physica B*, **180-181**, 1000-1002 (1992).
- [11] A.C. Larson and R.B. von Dreele, "General Structure Analysis System (GSAS)", *Los Alamos National Laboratory Report*, LAUR 86-748 (1994).
- [12] G. Azimi, H. Leion, M. Rydén, T. Mattisson and A. Lyngfelt, "Solid fuel conversion of iron manganese oxide as oxygen carrier for chemical looping with oxygen uncoupling (CLOU)", in "2nd International Conference on Chemical Looping", Darmstadt, Germany, (2012).

- [13] X. Zhan, V. Frick and H. Leion, "Determining CLOU reaction reactivity for combined manganese oxygen carriers and experimental issues during the work", in "40th International Technical Conference on Clean Coal and Fuel Systems", Clearwater, Florida, USA, (2015).
- [14] C.K. Clayton and K.J. Whitty, "Measurement and modeling of decomposition kinetics for copper oxide-based chemical looping with oxygen uncoupling", *Appl. Energy*, **116**, 416-423 (2014).

Table Captions.

Table 1. Summary of the crystallographic descriptions of the bixbyite, spinel and rocksalt crystal structures.

Table 2. Summary of the results of the least-squares refinements of the neutron diffraction data collected from bixbyite structured $(\text{Fe}_{0.2}\text{Mn}_{0.8})_2\text{O}_3$ at $700(2)^\circ\text{C}$ under 21% O_2 -79%Ar, spinel structured $(\text{Fe}_{0.2}\text{Mn}_{0.8})_3\text{O}_4$ at $900(2)^\circ\text{C}$ under 21% O_2 -79%Ar and rocksalt structured $(\text{Fe}_{0.2}\text{Mn}_{0.8})\text{O}$ at $760(2)^\circ\text{C}$ under 100%CO. The weighted profile and expected R -factors are given by

$$R_{\text{wp}}^2 = \sum_{N_d} \frac{(y_{\text{obs}} - y_{\text{calc}})^2}{(\sigma y_{\text{obs}})^2} \bigg/ \sum_{N_d} \frac{(y_{\text{obs}})^2}{(\sigma y_{\text{obs}})^2} \quad \text{and} \quad R_{\text{exp}}^2 = (N_d - N_v) \bigg/ \sum_{i=1}^{N_d} \frac{(y_{\text{obs}})^2}{(\sigma y_{\text{obs}})^2},$$

respectively, and the summations are made over the N_d data points used in the fit. N_v is the number of fitted variables. y_{obs} and y_{calc} are the observed and calculated intensities, respectively, and σy_{obs} is the estimated standard deviation on y_{obs} derived from the counting statistics.

| | | | |
|----------------------------------|---|---|--|
| Structure | Bixbyite | Spinel | Rocksalt |
| Space Group | $Ia\bar{3}$ | $Fd\bar{3}m$ | $Fm\bar{3}m$ |
| Stoichiometry | M_2X_3 | M_3X_4 | MX |
| Cations (M) per unit cell | 32 | 24 | 4 |
| Anions (X) per unit cell | 48 | 32 | 4 |
| <i>f.c.c.</i> sublattice | cations | anions | cations or anions |
| <i>oct.</i> sites per unit cell | 32 | 32 | 4 |
| <i>tet.</i> sites per unit cell | 64 | 64 | 8 |
| <i>f.c.c.</i> sites | $M1$ in $8(a)$ $0,0,0$, etc. $M2$ in $24(d)$ $x,0,1/4$, etc. with $x=1/4$ | X in $32(e)$ x,x,x , etc. with $x=1/4$ | M/X in $4(a)$ $0,0,0$, etc. |
| Octahedral (<i>oct</i>) sites | <i>oct1</i> in $8(b)$ $1/4, 1/4, 1/4$, etc. <i>oct2</i> in $24(d)$ $x,0,1/4$, etc. with $x=0$ | <i>oct1</i> in $16(c)$ $0,0,0$, etc. <i>oct2</i> in $16(d)$ $1/2, 1/2, 1/2$, etc. | <i>oct</i> in $4(b)$ $1/2, 1/2, 1/2$, etc. |
| Tetrahedral (<i>tet</i>) sites | <i>tet1</i> in $16(c)$ x,x,x , etc. with $x=1/8$ <i>tet2</i> in $48(e)$ x,y,z , etc. with $x=1/8, y=3/8,$ $z=1/8$ | <i>tet1</i> in $8(a)$ $1/8, 1/8, 1/8$, etc. <i>tet2</i> in $8(b)$ $3/8, 3/8, 3/8$, etc. <i>tet3</i> in $48(f)$ $x, 1/8, 1/8$, etc. with $x=3/8$ | <i>tet</i> in $8(c)$ $1/4, 1/4, 1/4$, etc. |
| Occupied sites | <i>tet2</i> | <i>oct2</i> and <i>tet1</i> | <i>oct</i> |

Table 1, Norberg, Azimi, Hull and Leion.

| | | | |
|--|---|---|--|
| Phase | $(\text{Fe}_{0.2}\text{Mn}_{0.8})_2\text{O}_3$ | $(\text{Fe}_{0.2}\text{Mn}_{0.8})_3\text{O}_4$ | $(\text{Fe}_{0.2}\text{Mn}_{0.8})\text{O}$ |
| Structure | Bixbyite | Spinel | Rocksalt |
| Space group | $Ia\bar{3}$ | $Fd\bar{3}m$ | $Fm\bar{3}m$ |
| Temperature ($^{\circ}\text{C}$) | 700(2) | 900(2) | 750(2) |
| Atmosphere | 21% O_2 -79%Ar | 21% O_2 -79%Ar | 100%CO |
| Lattice parameter, a (\AA) | 9.48780(8) | 8.61412(7) | 4.47737(4) |
| Unit cell volume, V_u (\AA^3) | 854.075(12) | 639.193(8) | 89.7572(12) |
| Vol. per $(\text{Fe}_{0.2}\text{Mn}_{0.8})\text{O}_x$ (\AA^3) | 26.6898(4) | 26.6330(3) | 22.4393(3) |
| Atom positions | $M1$ ($\text{Fe}_{1-m_{M1}}\text{Mn}_{m_{M1}}$) 8(a) 0,0,0, etc. $M2$ ($\text{Fe}_{1-m_{M2}}\text{Mn}_{m_{M2}}$) 24(d) $x_{M2}, 0, 1/4$, etc. O 48(e) $x_{\text{O}2}, y_{\text{O}}, z_{\text{O}}$, etc. | $M1$ ($\text{Fe}_{1-m_{M1}}\text{Mn}_{m_{M1}}$) 8(a) $1/8, 1/8, 1/8$, etc. $M2$ ($\text{Fe}_{1-m_{M2}}\text{Mn}_{m_{M2}}$) 16(d) $1/2, 1/2, 1/2$, etc. O 32(e) $x_{\text{O}}, x_{\text{O}}, x_{\text{O}}$, etc. | M ($\text{Fe}_{0.2}\text{Mn}_{0.8}$) 4(a) 0,0,0, etc. O 4(b) $1/2, 1/2, 1/2$, etc. |
| Positional parameters | $x_{M2}=0.2822(8)$ $x_{\text{O}}=0.08383(16)$ $y_{\text{O}}=0.3691(2)$ $z_{\text{O}}=0.1434(2)$ | $x_{\text{O}}=0.26263(8)$ | |
| Site occupancies | $m_{M1}=0.689(5)$ $m_{M2}=0.840(5)$ | $m_{M1}=0.864(8)$ $m_{M2}=0.763(3)$ | |
| Thermal parameters (\AA^3) | $u_{M1}=0.0013(3)$ $u_{M2}=0.0014(3)$ $u_{\text{O}}=0.00196(4)$ | $u_{M1}=0.0031(4)$ $u_{M2}=0.0011(4)$ $u_{\text{O}}=0.00367(5)$ | $u_{\text{M}}=0.00229(11)$ $u_{\text{O}}=0.00224(3)$ |
| Number of fitted parameters | 34 | 32 | 29 |
| Number of data points | 3314 | 3314 | 3314 |
| Weighted R -factor, R_{wp} (%) | 2.03 | 1.74 | 1.88 |
| Expected R -factor, R_{exp} (%) | 1.83 | 1.64 | 1.72 |
| Bond lengths (\AA) | $M1$ -O 2.0066(17) ($\times 6$) $M2$ -O 1.909(6) ($\times 2$) 2.045(5) ($\times 2$) 2.239(3) ($\times 2$) | $M1$ -O 2.0534(13) ($\times 4$) $M2$ -O 2.0505(6) ($\times 6$) | M -O 2.23869(2) ($\times 6$) |
| Bond angles ($^{\circ}$) | O- $M1$ -O 84.58(6) ($\times 6$) 95.42(6) ($\times 6$) 180.0 ($\times 3$) O- $M2$ -O 75.56(5) ($\times 2$) 77.99(4) ($\times 2$) 83.28(6) ($\times 2$) 92.71(3) ($\times 1$) 95.19(4) ($\times 2$) 103.17(6) ($\times 1$) 114.67(8) ($\times 2$) 136.82(11) ($\times 1$) 167.08(13) ($\times 2$) | O- $M1$ -O 109.47 ($\times 6$) O- $M2$ -O 83.77(4) ($\times 6$) 96.23(4) ($\times 6$) 180.0 ($\times 3$) | O- M -O 90.0 ($\times 12$) 180.0 ($\times 3$) |

Table 2, Norberg, Azimi, Hull and Leion.

Figure Captions.

Figure 1. Schematic diagram of Chemical-Looping with Oxygen Uncoupling (CLOU).

Figure 2. Phase diagram of $(\text{Fe}_{1-x}\text{Mn}_x)\text{O}_y$ calculated using the FactSage software and accompanied FToxid database [6,7], for a partial pressure of 5% O_2 (roughly corresponding to the exiting O_2 concentration from the air reactor).

Figure 3. Comparison of the Thermal Gravimetric Analysis (TGA) and Neutron Powder Diffraction (NPD) data for the weight loss of $(\text{Fe}_{0.21}\text{Mn}_{0.79})_2\text{O}_3$ and $(\text{Fe}_{0.2}\text{Mn}_{0.8})_2\text{O}_3$, respectively, when heated under an atmosphere of 5% O_2 .

Figure 4. The crystal structures of (a) bixbyite ($M_2\text{O}_3$), (b) spinel ($M_3\text{O}_4$) and (c) rocksalt (MO).

Figure 5. The evolution of a portion of the neutron powder diffraction pattern from $(\text{Fe}_{0.2}\text{Mn}_{0.8})_2\text{O}_3$ heated from 701°C to 956°C under an atmosphere of 100%Ar showing the transition from a mixed (bixbyite plus spinel) phase to a single spinel phased material.

Figure 6. The variation in the weight fraction of the spinel and bixbyite phases of $(\text{Fe}_{0.2}\text{Mn}_{0.8})_2\text{O}_3$ under atmospheres of (a) 100%Ar, (b) 21% O_2 -79%Ar and (c) 5% O_2 -95%Ar determined from the NPD data. The closed and open symbols refer to heating and cooling, respectively.

Figure 7. The evolution of a portion of the neutron powder diffraction pattern from $(\text{Fe}_{0.2}\text{Mn}_{0.8})_2\text{O}_3$ heated under CO at 848°C showing the formation of the rocksalt (R) structured phase and the subsequent reforming of the spinel (S) and bixbyite (B) structured phases at 760°C under O_2 .

Figure 8. Least-squares fits to the powder neutron diffraction data collected from (a) bixbyite structured $(\text{Fe}_{0.2}\text{Mn}_{0.8})_2\text{O}_3$ at 700(2)°C under 21% O_2 -79%Ar, (b) spinel structured $(\text{Fe}_{0.2}\text{Mn}_{0.8})_3\text{O}_4$ at 900(2)°C under 21% O_2 -79%Ar and (c) rocksalt structured $(\text{Fe}_{0.2}\text{Mn}_{0.8})\text{O}$ at 760(2)°C under 100%CO. The dots are the experimental data points (with the background from the silica sample container and furnace subtracted) and the solid lines are the calculated profiles using the parameters listed in table 2. The lower traces show the difference (measured minus calculated) divided by the estimated standard deviation on the experimental data points. The rows of tick marks along the top of the figures denote the calculated positions of all the symmetry allowed Bragg reflections for space groups $Ia\bar{3}$, $Fd\bar{3}m$ and $Fm\bar{3}m$, respectively.

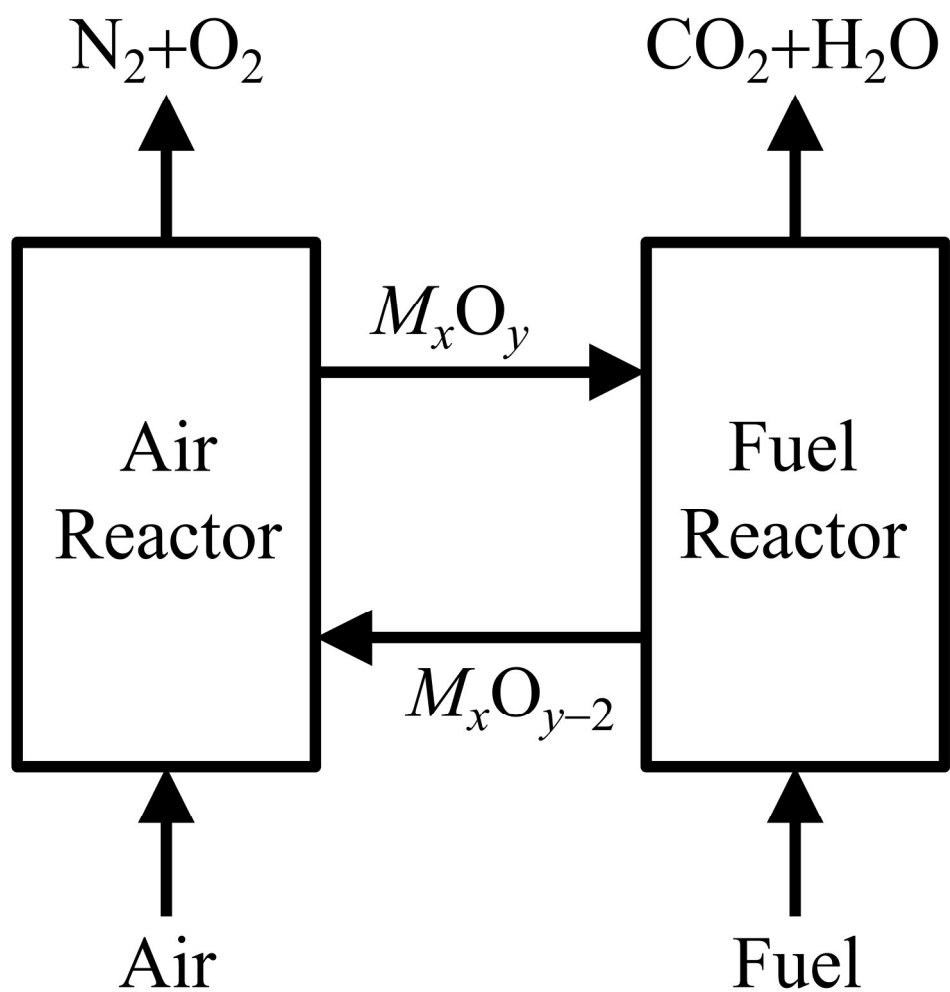
Figure 9. The variation of the unit cell volume per formula unit, V/Z , for the bixbyite and spinel phases of $(\text{Fe}_{0.2}\text{Mn}_{0.8})\text{O}_y$ with temperature. The symbols denote the atmosphere during each measurement (●, ▲ and ▼ refer to 21% O_2 -79%Ar, 100%Ar and 5% O_2 -95%Ar atmospheres, respectively) and the open/closed symbols indicate data collected under cooling/heating conditions.

Figure 10. The variation of the positional parameters x_{M2} , x_{O} , y_{O} , and z_{O} for the bixbyite phase of $(\text{Fe}_{0.2}\text{Mn}_{0.8})_2\text{O}_3$ with temperature. The symbols denote the atmosphere during each measurement (●, ▲ and ▼ refer to 21% O_2 -79%Ar, 100%Ar and 5% O_2 -95%Ar atmospheres, respectively) and the open/closed symbols indicate data collected under cooling/heating conditions.

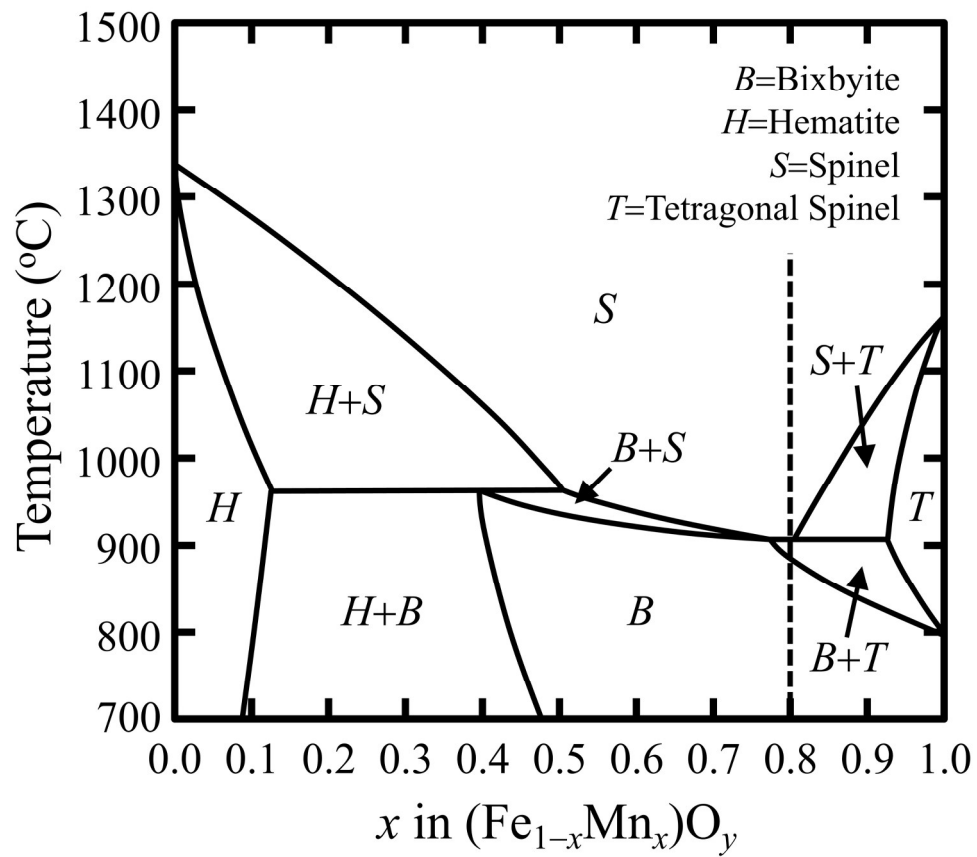
Figure 11. The variation of the isotropic thermal vibration parameters u_{M1} , u_{M2} and u_{O} for the bixbyite phase of $(\text{Fe}_{0.2}\text{Mn}_{0.8})_2\text{O}_3$ with temperature. The symbols denote the atmosphere during each measurement (●, ▲ and ▼ refer to 21% O_2 -79%Ar, 100%Ar and 5% O_2 -95%Ar atmospheres, respectively) and the open/closed symbols indicate data collected under cooling/heating conditions.

Figure 12. The variation of the Mn occupancy, m_M , for the $M1$ and $M2$ sites within the bixbyite $(\text{Fe}_{0.2}\text{Mn}_{0.8})_2\text{O}_3$ and spinel phases of $(\text{Fe}_{0.2}\text{Mn}_{0.8})_3\text{O}_4$ with temperature. The symbols denote the atmosphere during each measurement (●, ▲ and ▼ refer to 21% O_2 -79%Ar, 100%Ar and 5% O_2 -95%Ar atmospheres, respectively) and the open/closed symbols indicate data collected under cooling/heating conditions.

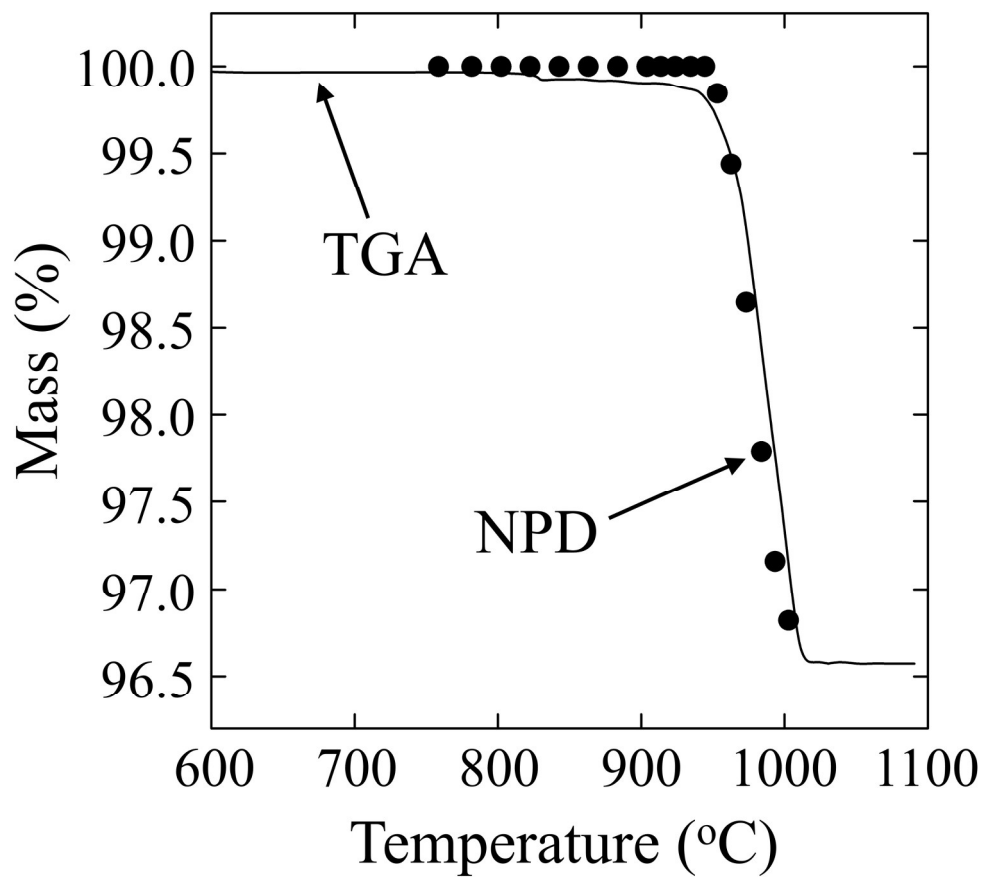
Figure 13. The variation of the positional parameter x_{O} , and the isotropic thermal vibration parameters u_{M1} , u_{M2} and u_{O} for the spinel phase of $(\text{Fe}_{0.2}\text{Mn}_{0.8})_2\text{O}_3$ with temperature. The symbols denote the atmosphere during each measurement (●, ▲ and ▼ refer to 21% O_2 -79%Ar, 100%Ar and 5% O_2 -95%Ar atmospheres, respectively) and the open/closed symbols indicate data collected under cooling/heating conditions.



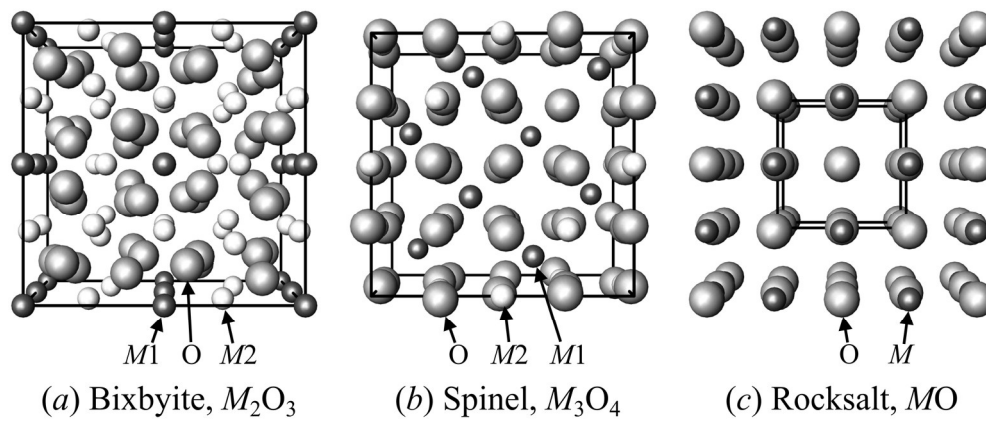
207x212mm (300 x 300 DPI)



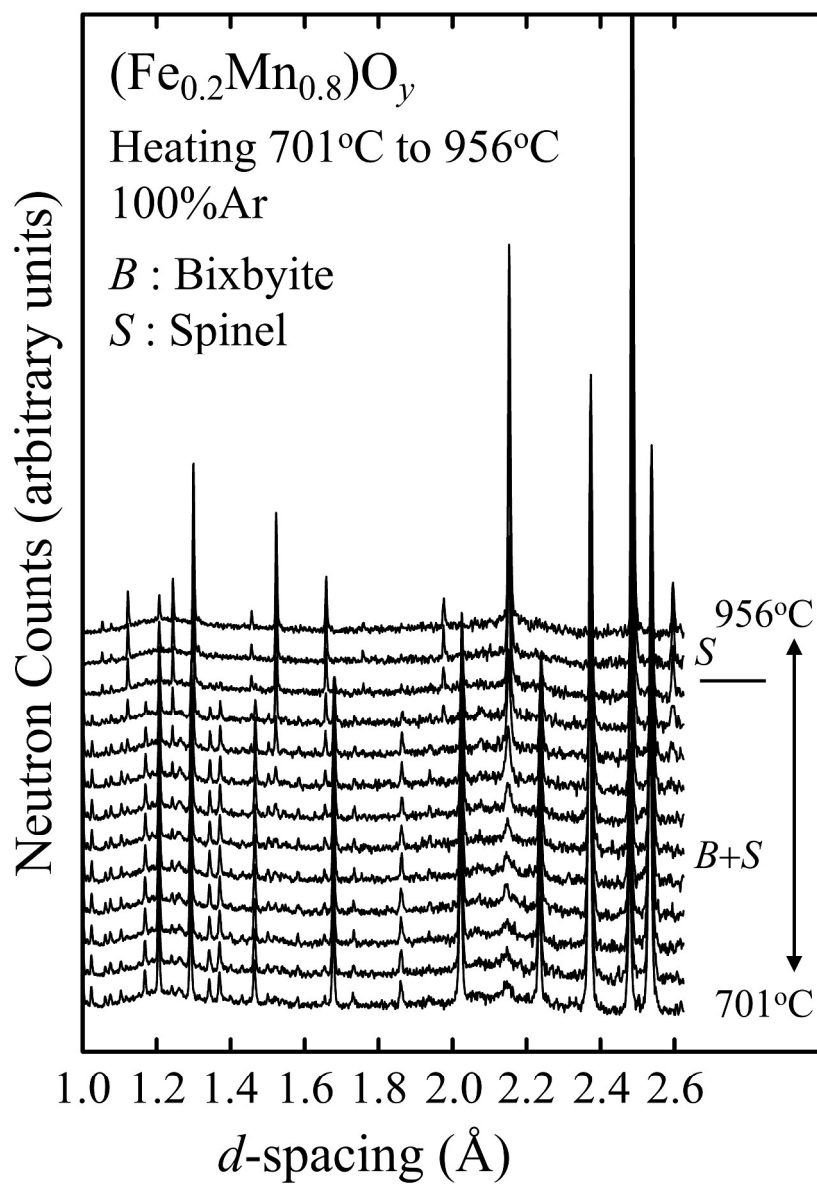
179x159mm (300 x 300 DPI)



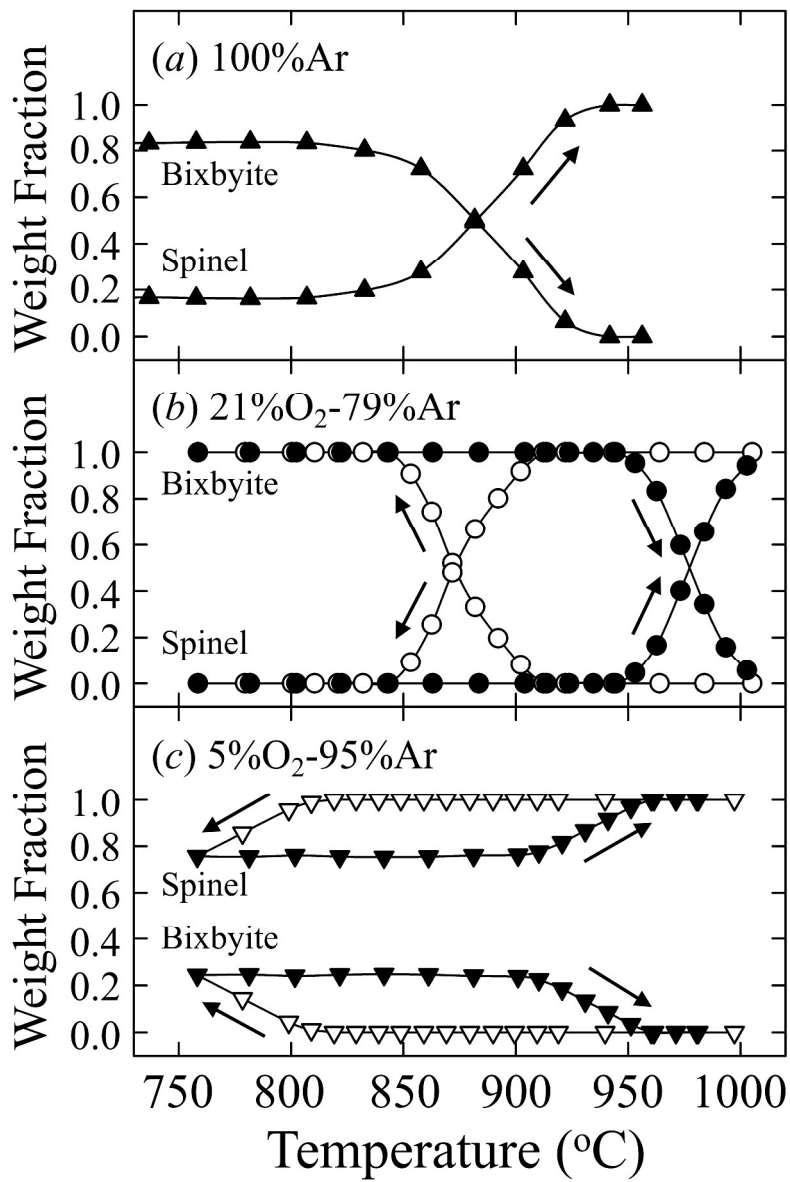
185x169mm (300 x 300 DPI)



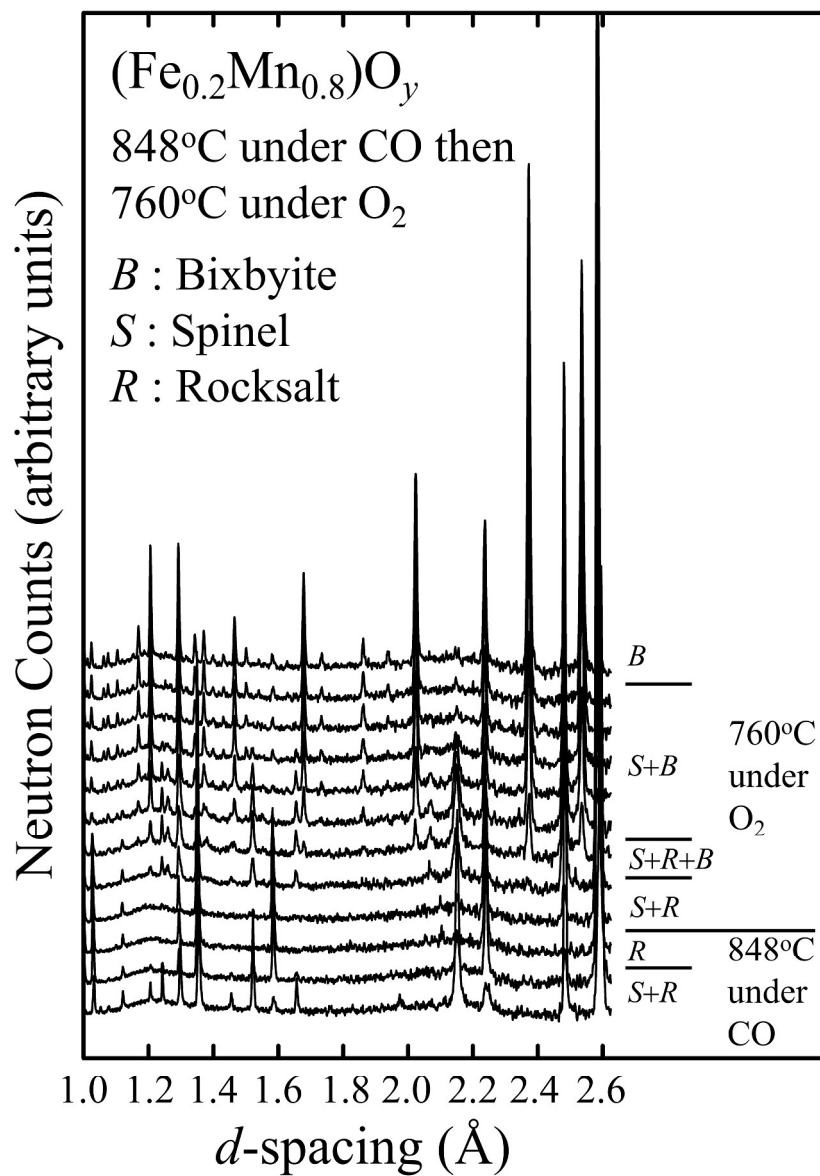
171x72mm (300 x 300 DPI)



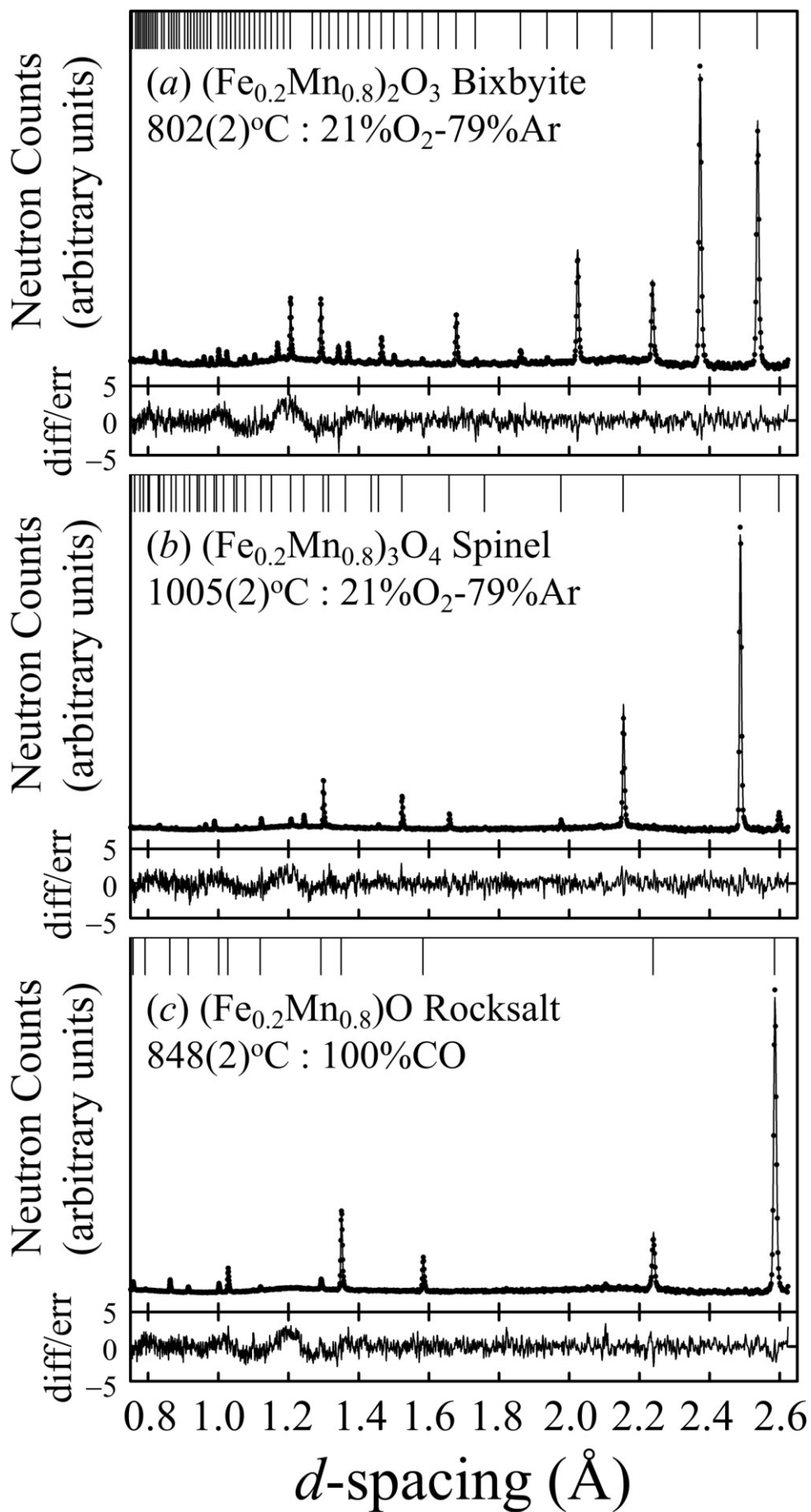
291x417mm (300 x 300 DPI)

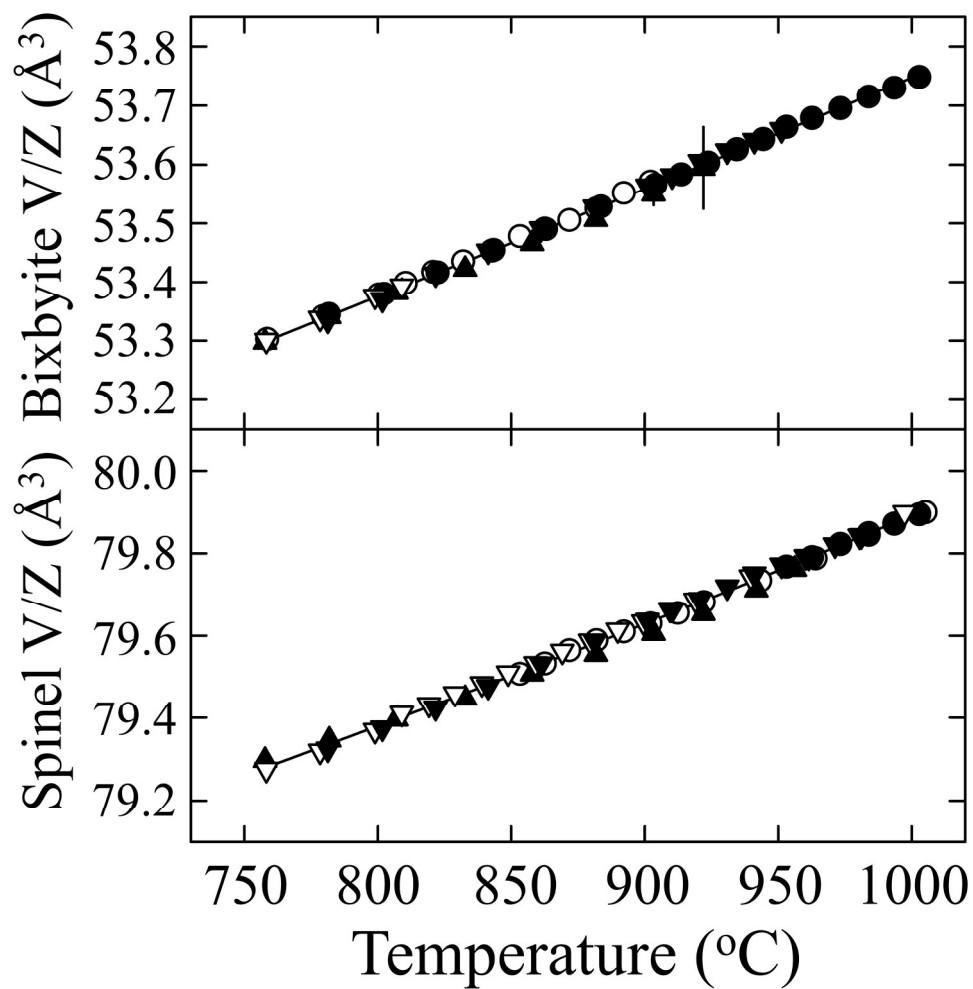


305x458mm (300 x 300 DPI)

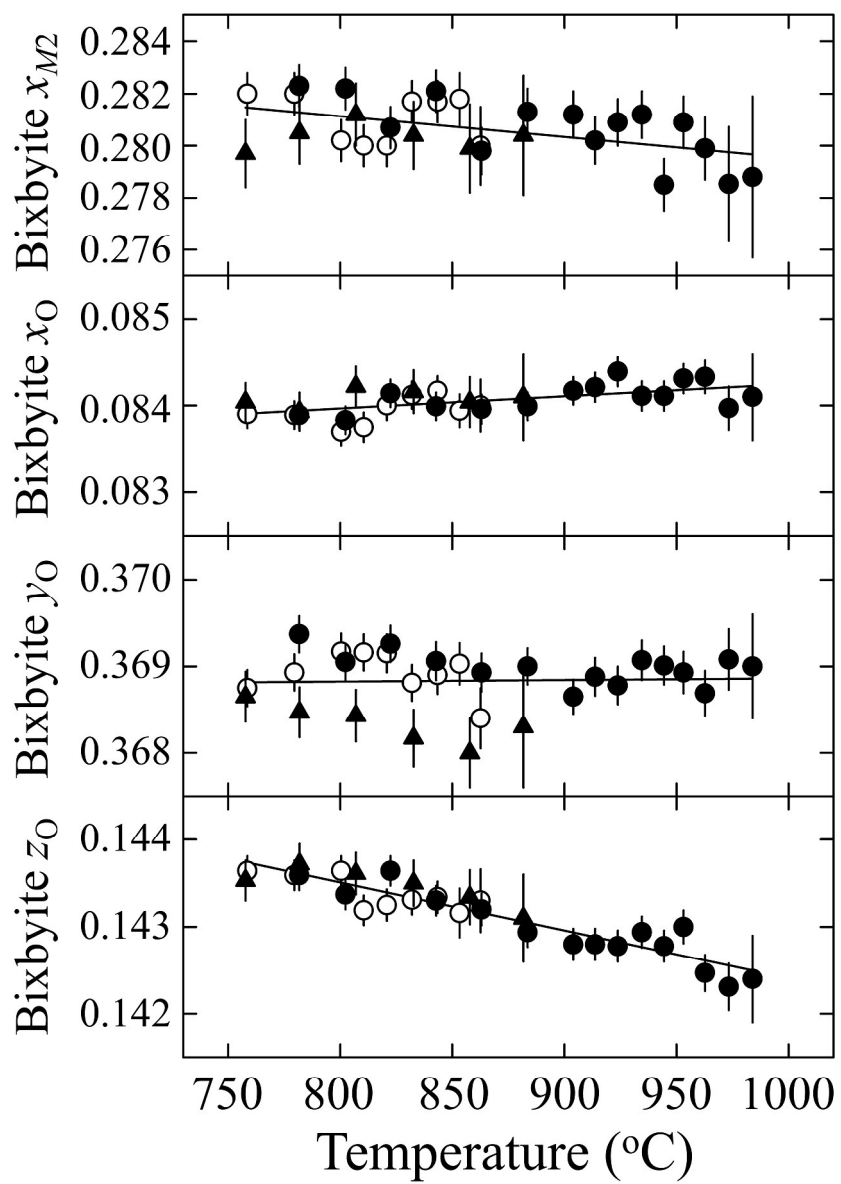


286x404mm (300 x 300 DPI)

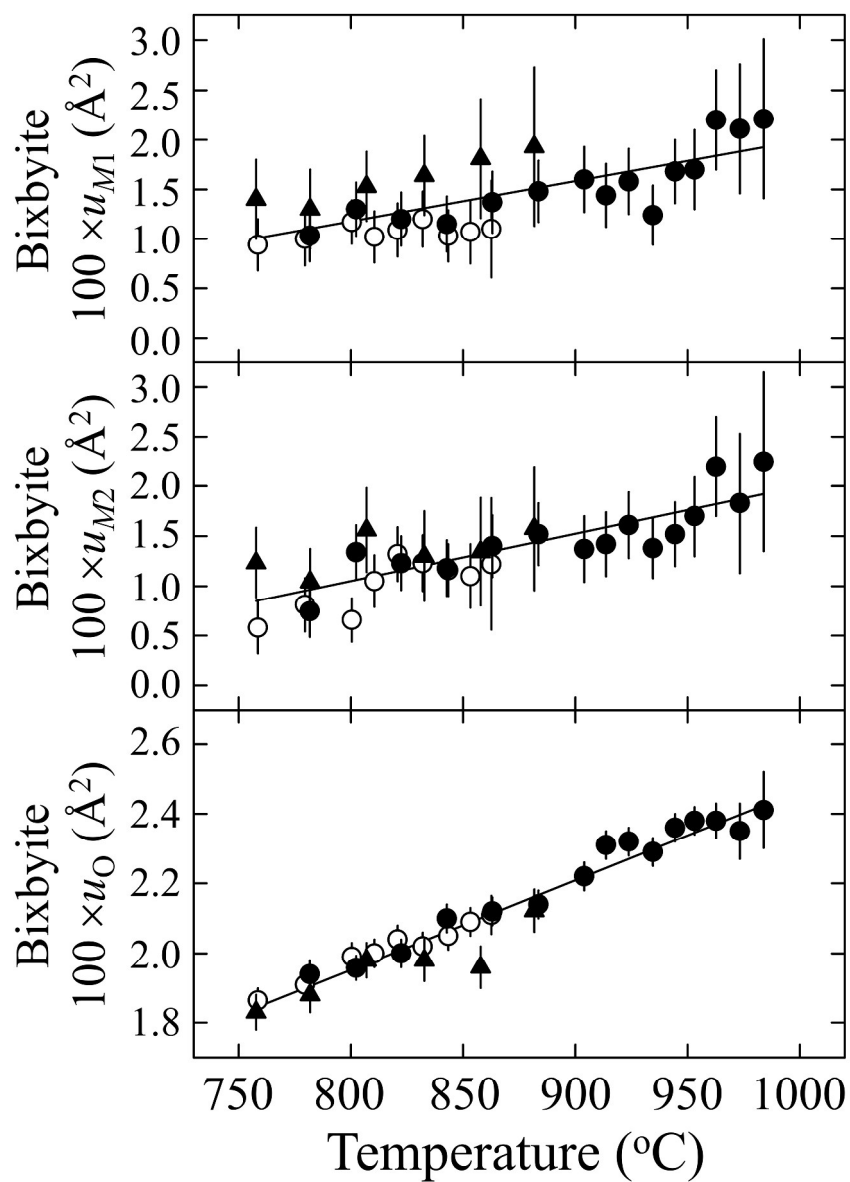




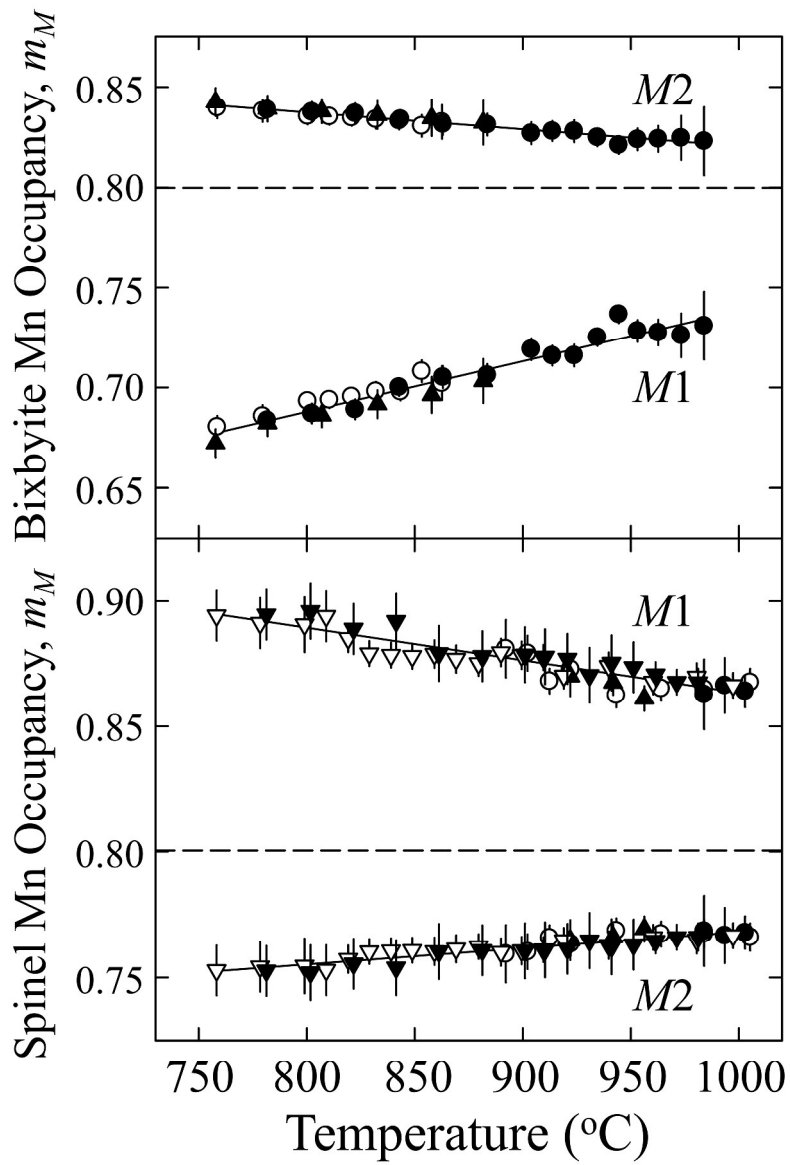
208x214mm (300 x 300 DPI)



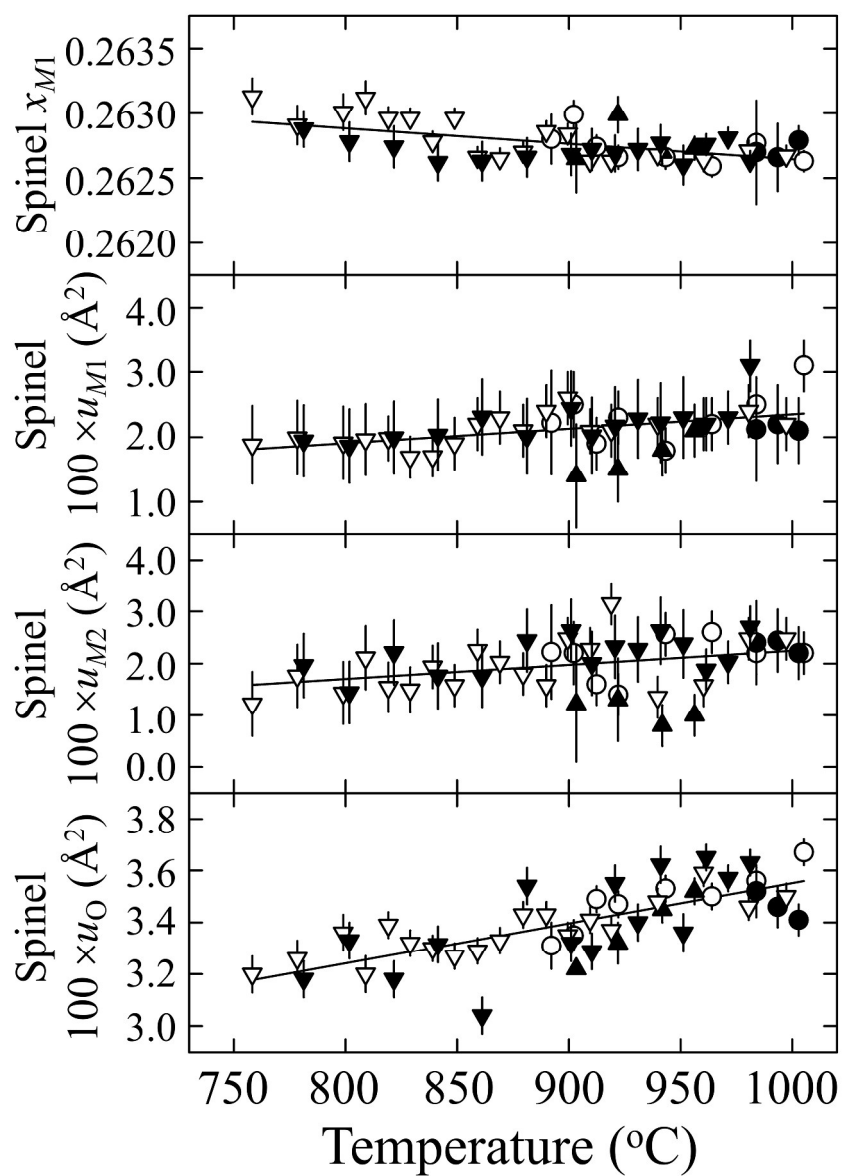
285x401mm (300 x 300 DPI)



283x396mm (300 x 300 DPI)



299x442mm (300 x 300 DPI)



285x399mm (300 x 300 DPI)